ACS OMEGA

Open Access

http://pubs.acs.org/journal/acsodf

Article

The Electrochemical and Structural Changes of Phosphorus-Doped TiO_2 through In Situ Raman and In Situ X-Ray Diffraction Analysis

Ayoub El Bendali, Mohamed Aqil, Loubna Hdidou, Nabil El Halya, Karim El Ouardi, Jones Alami, Davide Boschetto, and Mouad Dahbi*

Cite This: *ACS Omega* 2024, 9, 14911−14922

Read Online

ACCESS | Metrics & More | Article Recommendations | Supporting Information

ABSTRACT: Doping is a widely employed technique to enhance the functionality of lithium-ion battery materials, tailoring their performance for specific applications. In our study, we employed in situ Raman and in situ X-ray diffraction (XRD) spectroscopic techniques to examine the structural alterations and electrochemical behavior of phosphorus-doped titanium dioxide (TiO_2) nanoparticles. This investigation revealed several notable changes: an increase in structural defects, enhanced ionic and electronic conductivity, and a reduction in crystallite size. These alterations facilitated higher lithiation rates and led to the first observed appearance of $LiTiO_2$ in the Raman spectra due to anatase lithiation, resulting in a reversible double-phase transition during the charging and discharging processes. Furthermore, doping with 2, 5, and 10 wt % phosphorus resulted in an initial increase in specific capacity compared to undoped TiO_2. However, higher doping levels were associated with diminished capacity retention, pinpointing an optimal doping level for phosphorus. These results underscore the critical role of in situ characterization techniques in understanding doping effects, thereby advancing the performance of anode materials, particularly TiO_2, in lithium-ion batteries.

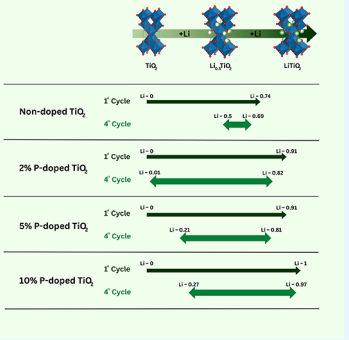

INTRODUCTION

The growing need for energy storage solutions across various sectors, including electronics, electric vehicles, and stationary storage, has propelled the advancement of high-performance lithium-ion batteries (LIBs).[1−3] These batteries consist of four primary components: the anode, cathode, separator, and electrolyte, with the anode being crucial for overall battery performance. Recent efforts have focused on developing efficient, cost-effective, and safe anode materials for LIBs.[4−6] Titanium dioxide (TiO_2) has emerged as a promising anode material, owing to its safety, versatile redox chemistry, affordability, and environmental sustainability.[7−9] Among the various TiO_2 structures, anatase is noteworthy, offering a specific capacity comparable to graphite (around 330 mAh g^{-1}) and a discharge voltage plateau near 1.7 V vs Li^+/Li. However, the performance of anatase is somewhat limited by the tetragonal $LiTiO_2$ phase, which impedes lithium-ion diffusion.[10,11]

During lithiation, a Li-poor tetragonal anatase Li_xTiO_2 with less than 0.03 and an $I41/amd$ space group forms initially. A second phase transition to the orthorhombic $Li_{0.55}TiO_2$ phase in the *Imma* space group occurs at $x = 0.55$, where only half the octahedral sites are filled with lithium ions.[10] At deeper lithiation stages, a tetragonal structure emerges when these octahedral sites are fully occupied.[12] The rapid advancement in nanostructured TiO_2 synthesis has led to various enhancements, such as optimized morphology, particle size,[13] porosity,[14] and carbon coating, all contributing to improved electrochemical behavior.

Notably, hierarchical structures with more exposed surfaces, open channels for electrolyte penetration, and shortened ion diffusion paths significantly impact the electrochemical activity. Wu et al. prepared petal-like TiO_2 with a particle size of 12 nm and a BET surface area of 28.4 m^2 g^{-1}, which demonstrated excellent cycling stability and a high specific charge capacity of 326 mAh g^{-1} at 20 mAh g^{-1}.[15] Similarly, TiO_2 nanowires have achieved a reversible capacity of about 305 mAh g^{-1}.[16] Furthermore, the study of 3D porous materials, with their high porosity and specific surface area, has been gaining traction. These materials can accommodate more Li-ions, offering higher capacities.[17] Despite these advancements, TiO_2's low electrical conductivity and poor rate capability remain challenges. Doping TiO_2 with elements like F, P, N, Zr, etc.[18,19] has been shown to enhance electrochemical performance by facilitating more channels and active sites for Li-ion transport. For instance, Sn-doped TiO_2 nanotubes exhibited higher capacities and improved performance compared to undoped versions.[20] TiO_2 was codoped with Zr^{4+}/F^- to

Received: October 27, 2023
Revised: December 15, 2023
Accepted: December 22, 2023
Published: March 22, 2024

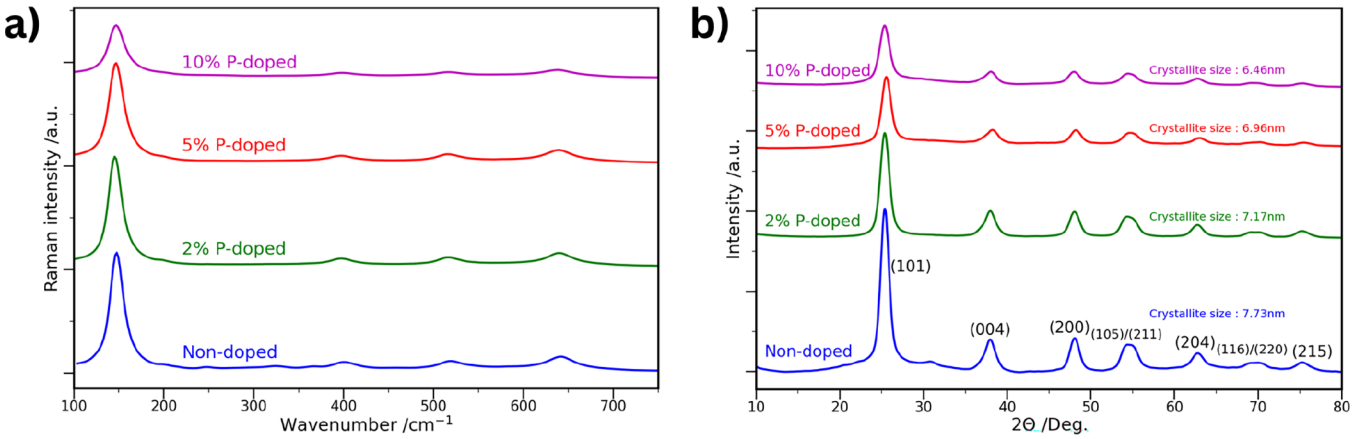

Figure 1. X-ray diffraction (XRD) and Raman spectrum of pristine and P-doped TiO_2: (a) XRD spectrum showing crystallite sizes for each doping level; (b) area-normalized Raman spectrum.

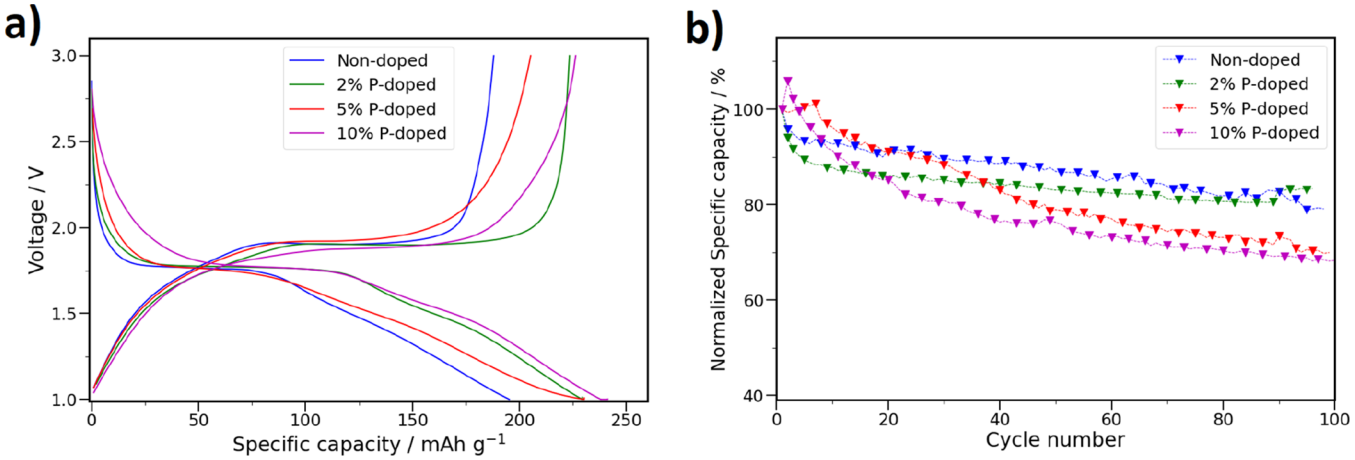

Figure 2. (a) Second-cycle voltage profiles for TiO_2 with varying P-doping levels, (b) capacity retention for TiO_2 at different P-doping levels, normalized to the capacity of the second cycle.

produce $Ti_{0.97}Zr_{0.03}O_{1.98}F_{0.02}$, which has a reversible capacity of 163 mAh g^{-1} at 1C but only 34 mAh g^{-1} when compared to $Ti_{0.97}Zr_{0.03}O_2$. The delithiation capacity of Zr^{4+}/F^- codoped TiO_2 is still as high as 138 mAh g^{-1} even at a cycling rate of 10C.[18] Phosphorus-doped TiO_2 synthesized using recycled human urine displayed an initial discharge capacity of 214 mAh g^{-1}, maintaining 159 mAh g^{-1} even after 100 cycles.[21,22]

In our study, we explored the structural changes in anatase TiO_2 and phosphorus-doped TiO_2 nanoparticles during lithiation and delithiation. Samples with varying P-doping percentages were prepared and evaluated as anode materials for lithium-ion batteries. We analyzed the impact of P-doping on the crystal structure and morphology using X-ray diffraction (XRD), scanning electron microscopy (SEM), and Raman spectroscopy. Additionally, in situ Raman spectroscopy and in situ XRD were employed to investigate the operational mechanism of titanium oxide during charging and discharging as well as the influence of doping on the lithiation process.

RESULTS

Characterization of the P-Doped TiO_2. The XRD pattern and Raman spectrum of P-doped TiO_2 are depicted in (Figure 1). The four analyzed materials primarily consist of anatase TiO_2. The nondoped TiO2 shows pronounced crystallinity, with distinct peaks at 2θ values of 25.37°, 37.97°, 48.06°, 54.22°, 54.53°, 62.59°, 68.97°, 70.07°, and 75.15°. These peaks correspond to the anatase planes (101), (004), (200), (105), (211), (204), (116), (220), and (215). A similar peak pattern is observed in phosphorus-doped TiO_2 nanoparticles. In the nondoped sample, minor traces of brookite TiO_2 are identified by a peak at approximately 30.84° in the XRD pattern and weak Raman bands between 240 and 370 cm^{-1}. These brookite traces are absent in P-doped TiO_2. The crystallite sizes for all samples were calculated using the Debye−Scherrer formula, focusing on the (110) peak, and included in the figure. Pure TiO_2 showed a crystallite size of 7.7 nm, whereas the 2%, 5%, and 10% P-doped samples exhibited sizes of 7.2, 7.0, and 6.5 nm, respectively. This reduction in crystallite size leads to peak broadening in the XRD patterns and more phonon confinement, as evidenced by the broadening of the Raman peaks.[23] The peak fitting of all the Raman spectra as well as the peaks' positions and fwhm are presented in Figure S2 and Table S1, the results confirm the phonon confinement by the increasing fwhm and red-shift of the Raman bands.

To evaluate the effect of phosphorus doping on the electrochemical performance of TiO_2 nanoparticles, cells were fabricated with TiO_2 and P-doped TiO_2 (2%, 5%, and 10%) as anodes. The second cycle galvanostatic voltage profiles (Figure 2-a) indicate that the discharge capacity and

https://doi.org/10.1021/acsomega.3c08122
ACS Omega 2024, 9, 14911−14922

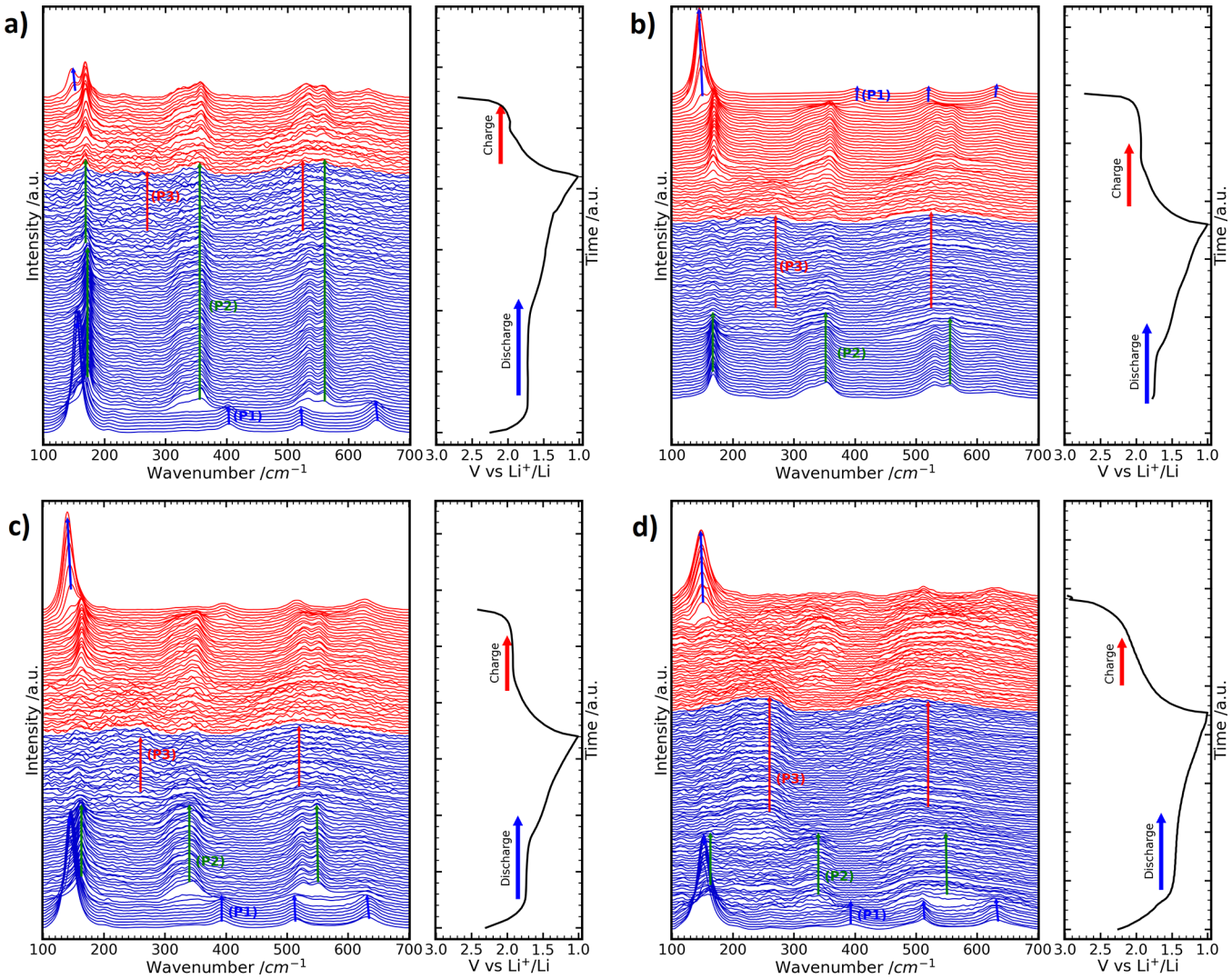

Figure 3. In situ Raman spectra of TiO_2 and P-doped TiO_2 anatase during the first lithiation and delithiation processes: (a) nondoped TiO_2, (b) 2% P-doped TiO_2, (c) 5% P-doped TiO_2, and (d) 10% P-doped TiO_2.

Coulombic efficiency, along with lithiation reversibility, improve with increasing doping levels. However, capacity retention analysis (Figure 2b) shows that 2% P-doping offers the best retention, which is clearer in the non-normalized capacity retention presented in (Figure S3), suggesting a slight doping enhances long-term reversibility without significantly affecting capacity loss in the initial cycles. In contrast, higher doping levels correlate with a consistent decrease in capacity retention despite initially higher capacities. Therefore, the optimal P-doping level for these materials appears to be around 2%, striking a balance between increased capacity and maintained capacity retention.

In situ Raman analysis on various P-doping levels of nanosized TiO_2 was conducted to investigate crystal structure changes and electrochemical reactivity during lithium insertion/extraction. This examination provides a comprehensive understanding of the behavior of these materials under different conditions.

In Situ Raman Investigation of P-Doped TiO_2 in the First Cycle. In the initial cycle, the in situ Raman results for the TiO_2 electrode (shown in Figure 3a) align with previous observations by Hardwick et al.[24] The emergence of Raman active modes A1g, 3Eg, and 2B1g around 1.75 V versus Li^+/Li signals the formation of the first Li-poor tetragonal anatase Li_xTiO2 phase (P1), identified by bands at 141 (Eg), 195 (Eg), 396 (B1g), 512 (A1g), 522 (B1g), and 628 cm^{-1} (Eg). Lithium insertion leads to shifts in TiO_2 anatase (P1) bands – the strong (Eg) band shifts to a higher wavenumber, while other bands exhibit red shifts, continuing until x = 0.07. Further lithium insertion results in a gradual decrease of the (P1) phase bands until the (Eg) band disappears, coinciding with the onset of a voltage profile plateau at approximately 1.75 V, marking the transition to the orthorhombic $Li_{0.5}TiO_2$ (P2) phase, indicated by new Raman bands.

In 2% and 5% P-doped TiO_2 materials (Figure 3b,c), similar phase transformations occur. Notably, the Raman measurement for the 2% P-doped sample did not commence at the start of discharge, but spectral analysis and reaction reversibility confirm the initial presence of the Li-poor anatase phase. As lithium insertion continues, the intensity of the (P2) phase bands diminishes and broadens, with weak, wide peaks emerging in the 200–300 cm^{-1} range and near 520 cm^{-1}. These are attributed to the Li-rich $LiTiO_2$ phase (P3). Previous studies report that this phase's formation on particle surfaces hinders full anatase $Li_{0.5}TiO_2$ lithiation due to low ionic conductivity.[8,10,25] At the discharge end, (P2) and (P3)

https://doi.org/10.1021/acsomega.3c08122
ACS Omega 2024, 9, 14911−14922

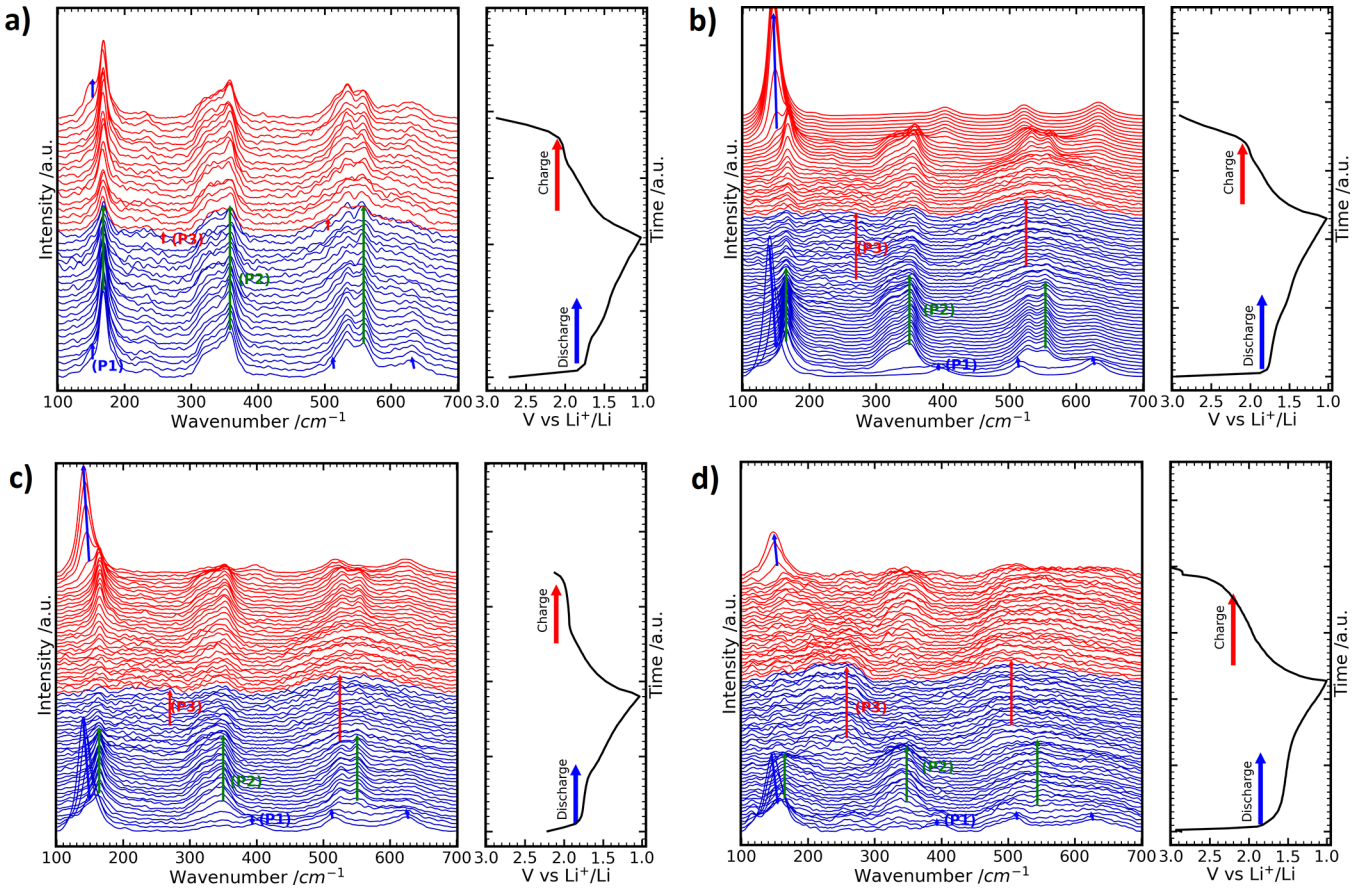

Figure 4. In situ Raman spectra of TiO_2 and P-doped TiO_2 anatase during the fourth lithiation and delithiation reactions: (a) nondoped TiO_2, (b) 2% P-doped TiO_2, (c) 5% P-doped TiO_2, and (d) 10% P-doped TiO_2.

phases coexist, with (P3) phase Raman spectra being less distinct. Gentili et al. and Hardwick et al. also observed this Li-rich phase with extremely weak Raman bands, suggesting only a minor amount of the orthorhombic (P3) phase.[11,24] However, in 2% and 5% P-doped TiO_2, the Li-rich phase (P3) is more pronounced at the discharge end, indicating that P-doping enhances titanium oxide's ionic conductivity, leading to deeper and more reversible lithiation. This is evidenced by the clearer Raman spectra of the (P3) phase in (Figure 3b,c), The effect is more pronounced in 5% P-doped TiO_2, suggesting better conductivity enhancement. Also, this is the first reported clear Raman spectra of the Li-rich TiO_2 phase (P3).[11] Moreover, in the 10% P-doped material (Figure 3d), The third phase (P3) was clearly visible after the voltage plateau at 1.5 V with no traces of the (P2) phase as observed in the 2% and 5% P-doped materials. This shows that higher lithiation levels are achieved due to a high P-doping ratio and therefore confirms the increase in the obtained first discharge capacity (Figure 2).

During the charging process and lithium extraction, the phase transitions are reversed and the (P2) peak reappears and becomes stronger. However, in nondoped material, the (P2) phase does not fully vanish at the charge end, highlighting TiO_2 anatase's limited reversibility, a finding supported by Hardwick et al.[24] Conversely, P-doped titanium oxides exhibit significantly improved reversibility, with the tetragonal non-lithiated TiO_2 phase fully reappearing at th charge end and no orthorhombic phase (P2) traces, explaining the increased first columbic efficiencies in P-doped materials (Figure 2).

The Raman bands for all phases are broader in 5% P-doped TiO_2 than in 2% P-doped TiO_2, implying larger crystallite size and lower structural defects in the 2% P-doping material.[26] The 10% P-doped material shows slight improvements in the lithiation reaction compared to the 2% and 5% P-doped materials, with broader Raman peaks due to the smaller crystallite size. At the charge end, traces of the third phase are still visible.

In summary, P-doping enhances lithiation levels by improving the ionic conductivity of the third phase (P3) of $LiTiO_2$, overcoming challenges to full lithiation.[25]

In Situ Raman of P-Doped TiO_2 in the Fourth Cycle. The Raman spectrum during the fourth cycle of the nondoped TiO_2 (Figure 4a) reveals coexistence of both the Li-poor tetragonal anatase (P1) and orthorhombic $Li_{0.5}TiO_2$ (P2) phases at the beginning of discharge. This observation indicates partial irreversibility, as some lithium ions inserted during the first cycle were not fully extracted. Notably, although the (P1) phase disappears early during lithium insertion and reemerges near 3 V at the end of charging, the (P2) phase remains predominant. Additionally, the Li-rich $LiTiO_2$ phase (P3) becomes evident near 500 cm^{-1} toward the end of lithiation at approximately 1 V, suggesting that TiO_2 does not achieve full lithiation. The dominance of the (P2) phase and the incomplete lithiation/delithiation reversibility contribute to the lower capacity of nondoped TiO_2 compared to its P-doped counterparts.

In contrast, the P-doped TiO_2 maintains a reversible reaction during cycling (Figure 4b,c). At the end of the charge

https://doi.org/10.1021/acsomega.3c08122
ACS Omega 2024, 9, 14911−14922

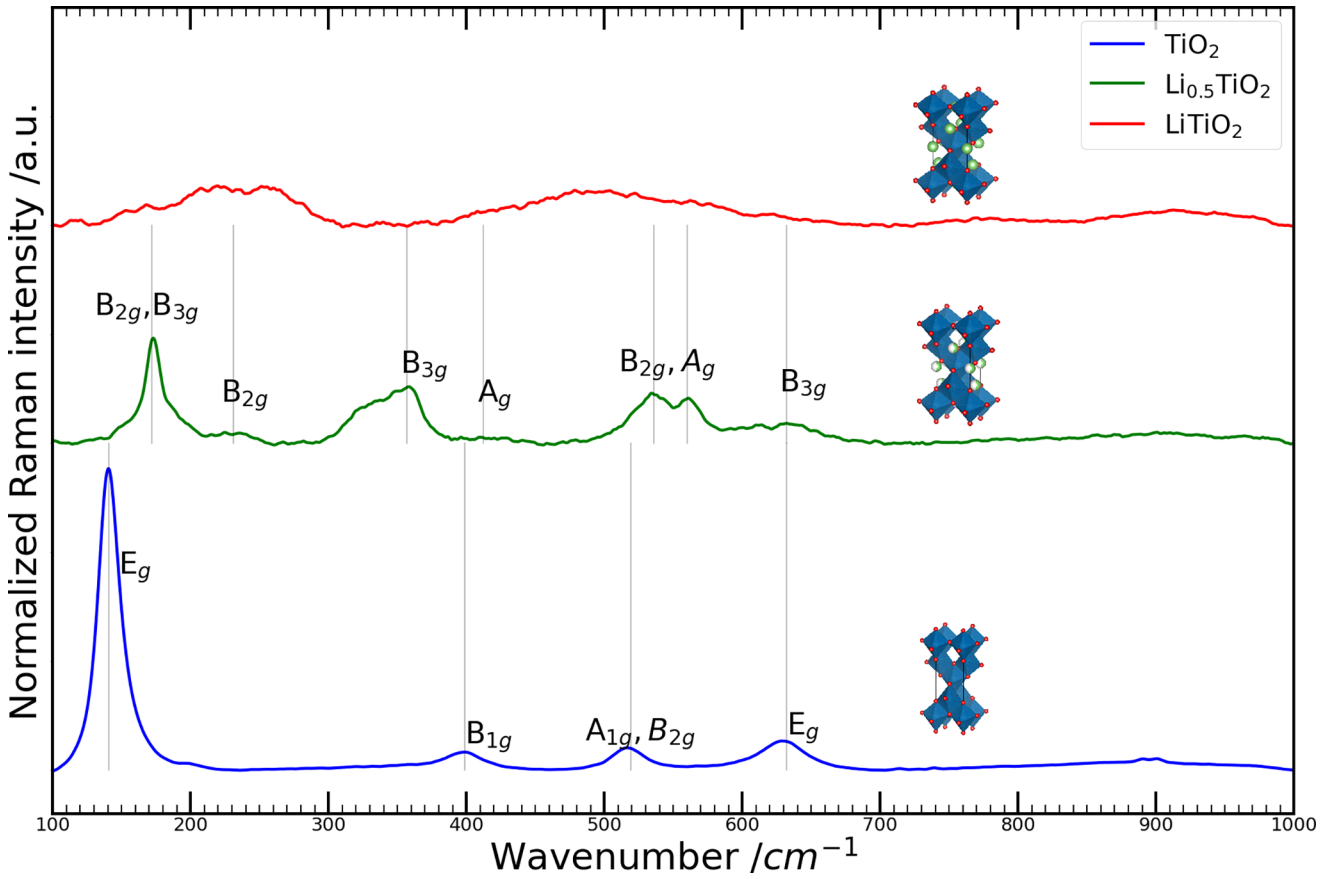

Figure 5. Raman spectra of lithiated TiO_2 generated by hierarchical clustering of the in situ Raman spectroscopy data for $x = 0$, $x = 0.5$, and $x = 1$.

process of the 2% P-doped TiO_2, only (P1) vibration bands were seen, indicating complete delithiation of the material. Furthermore, the Li-rich (P3) phase is consistently achieved at lower voltages (1 to 1.5 V vs Li^+/Li), though the (P2) phase bands remain present in the 5% P-doped TiO_2. This suggests a lithiation level of x varying from 0 to nearly 0.9, particularly at the particle surface. Despite not reaching theoretical capacity, possibly due to larger particle sizes (around 100 nm), significant improvements are observed compared to nondoped TiO_2, which achieves theoretical capacity only with small particles around 7 nm.[7]

The analysis of 10% P-doped TiO_2 (Figure 4d) shows favorable reversibility across all three phases. However, the broadened peaks across all phases indicate very low crystallinity and substantial structural defects.[27] Traces of the (P3) phase are present in the background of all spectra in the fourth cycle. Due to area normalization and relative weakness compared to the (P1) and (P2) phase spectra, the (P3) phase is less distinct. However, its presence will be further elucidated through hierarchical clustering and linear regression analysis of each spectrum against the Raman spectra of the phases. The deep lithiation observed in the 10% P-doped TiO_2leads to higher initial capacities but reduced cycling stability, which is attributed to significant volume expansion during lithium-ion insertion. This phenomenon explains the lower capacity retention observed in highly P-doped materials (Figure 2).

Quantification of Phases upon Cycling. The data from the in situ Raman spectroscopy of TiO_2 and P-doped TiO_2, collected over the first four cycles, was processed using Python. This involved organizing, smoothing, background subtraction, normalization, and peak detection within each spectrum. Python's flexibility and toolset enabled more detailed data extraction, including phase detection and changes during cycling. The methodologies and specific Python packages used are elaborated in the Methods section.

A key tool in detecting the existing phases is hierarchical clustering (HC). Utilizing $1 - c$ (where c is the correlation) as the distance measure, HC was applied to all spectra. The linkage distance threshold was adjusted to prevent misclassification of the combined spectra as new phases, and outlier clusters with only two or three spectra were disregarded.

The HC analysis identified three distinct clusters of spectra. For each cluster, one spectrum was chosen as representative, based on the maximum sum of correlations within its cluster and minimum correlation with spectra from other clusters. These representative spectra for each phase are shown in (Figure 5), and their peak fitting is presented in (Figure S2). The blue spectrum represents the nonlithiated anatase TiO_2 phase, identifiable at high voltages near 3 V. Peak fitting using a Lorentzian distribution identified five Raman modes observed at 141, 396, 512, 522, and 629 cm^{-1} in addition to a visible one around 200 cm^{-1} consistent with recent studies.[28] Two small peaks around 890 and 900 cm^{-1} are attributed to the electrolyte, similarly to the results reported by Hardwick et al. The second spectrum is attributed to the orthorhombic $Li_{0.5}TiO_2$ phase, corresponding to the plateau at 1.75 V. It was investigated by many recent works.[11,24,29] The peak fitting of the spectrum discerns 16 Raman bands at 97, 127, 153, 173, 190, 224, 238, 321, 335, 348, 360, 419, 534, 563, 605, 638, 810, 907, and 973 cm^{-1}. Laskova et al.[29] have theorized 42

https://doi.org/10.1021/acsomega.3c08122
ACS Omega 2024, 9, 14911−14922

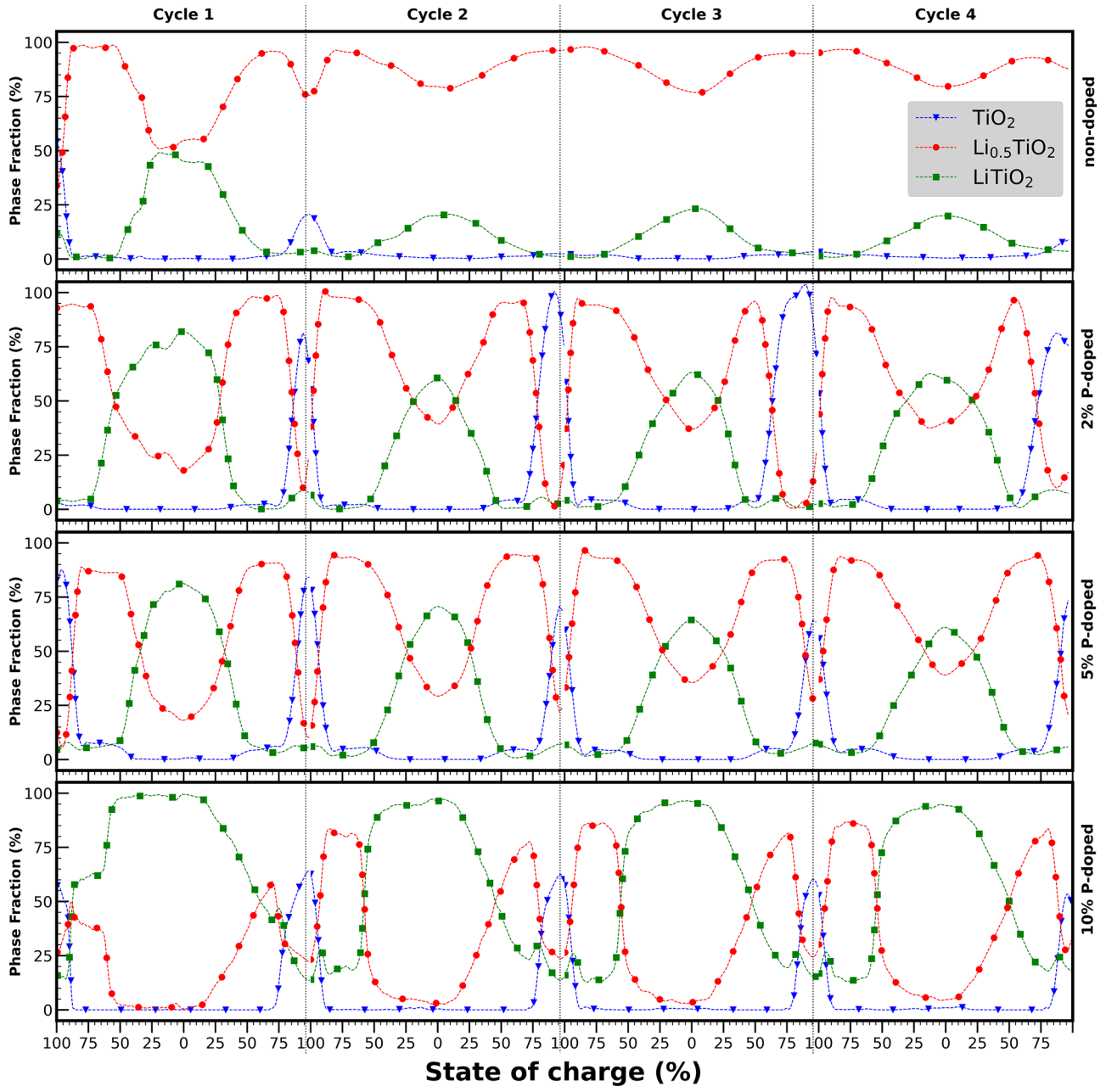

Figure 6. Change of phase fraction of the three phases of TiO_2 over cycling in the different P-doping levels.

Raman active vibrations ($14A_g + 14B_{1g} + 7B_{2g} + 7B_{3g}$) using DFT calculations for orthorhombic $Li_{0.5}TiO_2$, which is higher than 9 modes ($3A_g + 3B_{2g} + 3B_{3g}$) predicted by Hardwick et al.[24] using factor group analysis. Using the experimental spectra, 20 modes are detected, the peak positions are very similar, but there are still many differences, the B_{1g} and B_{2g} peaks at around 172 cm^{-1} are not separated as in previous works,[11,24,29] and the B_{2g} peak at 237 cm^{-1} has weaker intensity but appears more on the (P3) phase.

The third (red) spectrum is attributed to the tetragonal $LiTiO_2$ phase, appearing at lower voltages near 1 V and toward the end of the voltage profile. This spectrum is weaker, especially in nondoped TiO_2, with Lorentzian peak fitting revealing 12 peaks. Some peaks of the orthorhombic phase are visible in the background, but new, stronger peaks are observed around 213, 260, and 491 cm^{-1}, which are the main characteristics of this phase; the broadness of these peaks means that they can be composed of many other peaks, but the weakness of the entire spectra is insufficient to characterize them.

Raman spectroscopy, a robust vibrational spectroscopic method, was employed for quantitative phase analysis.[30] Linear regression was used with the Raman spectra of the three identified phases to determine phase fraction changes during charge/discharge cycles. For each spectrum measured during delithiation, linear coefficients for the three phases were calculated and normalized to sum to 1, estimating the phase fraction. It is important to note that this analysis is most reliable when coefficients are near 100% for one phase and 0% for the others; intermediate values provide comparative rather than absolute data. The state of charge was linearly calculated from the material's charge, associating a 100% state of charge at 3 V and 0% at 1 V.

https://doi.org/10.1021/acsomega.3c08122
ACS Omega 2024, 9, 14911−14922

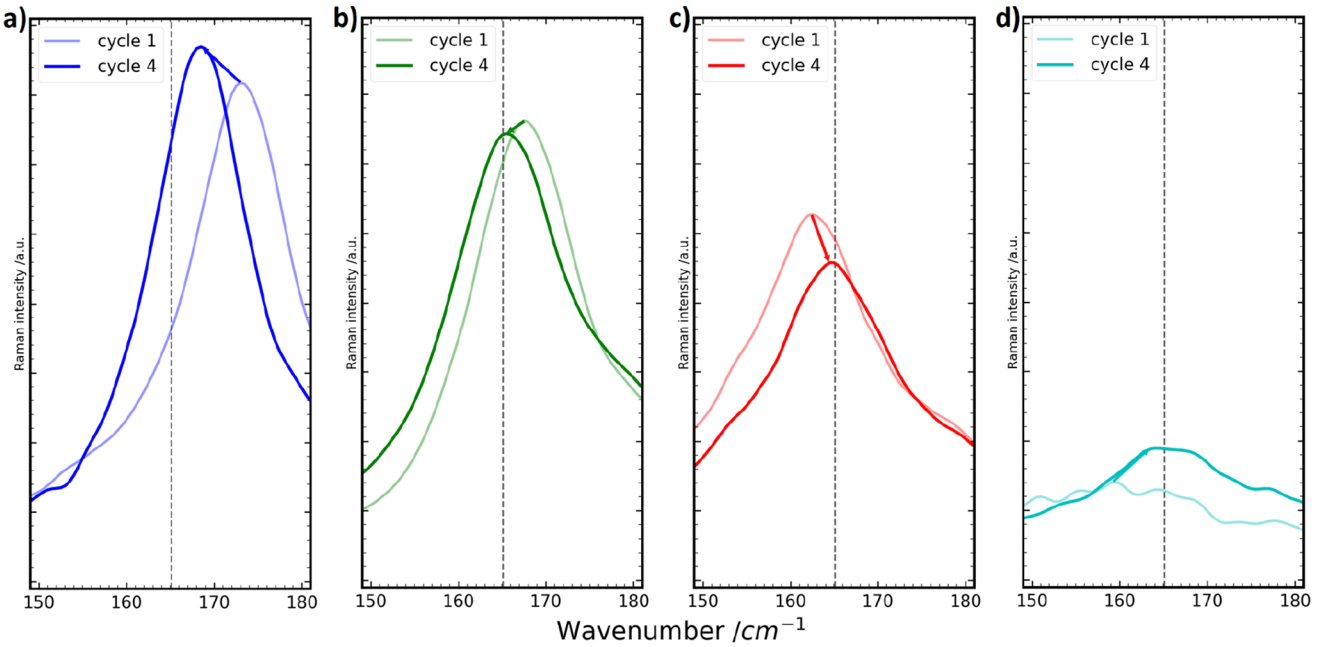

Figure 7. Comparison of the B_{2g}, B_{3g} band of the $Li_{0.5}TiO_2$ for P-doped TiO_2 between the first and the 4th cycle. (a) non doped TiO_2, (b) 2% p-doped TiO_2, (c) 5% p-doped TiO_2, (d) 10% p-doped TiO_2.

The linear regression results in Figure 6 are in accordance with the results described in Figure 3. Initially, all materials exhibit similar behavior, particularly during the first discharge. However, with increased P-doping levels, TiO_2 materials achieve higher lithiation states. Over repeated cycles, the fraction of the tetragonal $LiTiO_2$ phase increases with higher phosphorus doping levels. Notably, the highly doped material does not fully revert to the pure anatase phase at a 100% state of charge, hinting at long-term performance degradation and lower capacity retention, as observed in Figure 2. Particularly in 10% P-doped TiO_2, increased cycling leads to deeper lithiation, potentially reducing conductivity due to significant unit cell volume changes and a loss of electrical contact between particles.

The Effect of Phosphorus-Doping Level on the Vibrational Modes of $Li_{0.5}TiO_2$. During the first cycle, as depicted in Figure 7. The overlapped B_{2g} and B_{3g} bands of the $Li_{0.5}TiO_2$ phase at the different P-doping percentages were compared during the charge process of the first and fourth cycles. In the first cycle, with increasing P-doping, these bands shift toward lower wavenumbers and their intensities significantly decrease. This phenomenon is likely due to reduced particle size and increased structural defects. (Facile Li diffusion) Phonons interact with charge carriers through electron−phonon coupling. The increase of the material conductivity shortens the photons lifetime and causes bands broadening and the intensities to decrease.[31−34]

During the subsequent delithiation processes, lithium ions are easily extracted from the material's surface, but some remain trapped within the inner core,[35,36] the solid electrolyte interphase (SEI),[37] and/or in the Li-rich $LiTiO_2$ phase. This irreversibly trapped lithium acts as a doping agent, causing changes in the Raman bands. Particularly, peak positions for both nondoped TiO_2 and P-doped TiO_2 were observed to converge to around 165 cm^{-1}. For the nondoped and the 2% P-doped the band shifts to lower wavenumbers, which can be assigned to the effect of the lithium-ion trapped in the structure. For 5% and 10% P-doped TiO_2, the peak was blue-shifted, and this can be attributed to the effect of phosphor doping.

The vibrational modes of the $Li_{0.5}TiO_2$ crystal structure can be affected by dopants and/or impurities that disrupt the crystal lattice symmetry. Figure 7 shows that trapped lithium ions induce stress, evidenced by the red shift of these bands, contrasting with the blue shift caused by phosphorus doping. The shift of the peak between the first and fourth cycles is shown in Figure 8. An optimal P-doping level is identified

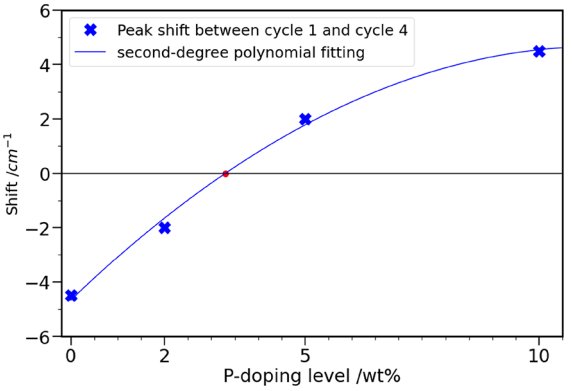

Figure 8. B_{2g}, B_{3g} band wavenumber change between the first cycle and the 4th cycle.

around 3.3 wt % (highlighted in red), where the combined effects of trapped lithium-ion and P-doping result in minimal peak movement during cycling.

Another effect, which is the intensity change and broadening, is observed in Figure 7, for the nondoped, 2% and 5% P-doped materials $Li_{0.5}TiO_2$ the change is due to the conductivity change of the material which causes a change in the phonon lifetime due to the phonon−electron coupling. The increasing intensity of nondoped anatase is caused by the decreasing conductivity due to the creation of the insulating $LiTiO_2$

https://doi.org/10.1021/acsomega.3c08122
ACS Omega 2024, 9, 14911−14922

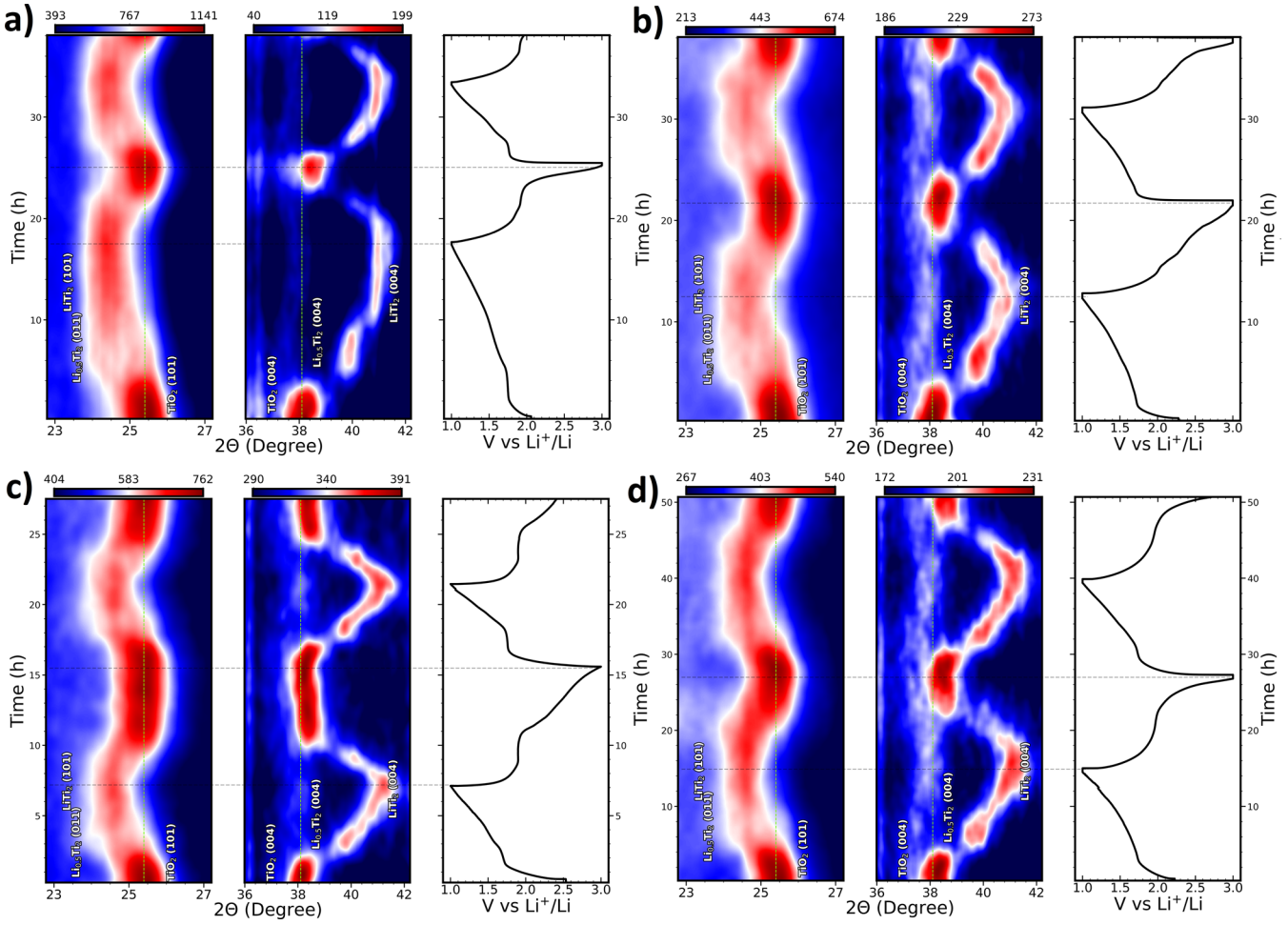

Figure 9. In situ XRD of TiO_2 and P-doped TiO_2 anatase during the first two lithiation and delithiation reactions. (a) non doped TiO_2, (b) 2% p-doped TiO_2, (c) 5% p-doped TiO_2, and (d) 10% p-doped TiO_2.

mainly on the surface. P-doping activation by lithiation causes intensity reduction and slight broadening, increasing the material's conductivity. However, at high P-doping levels, conductivity decreases due to extensive lithiation, leading to significant unit cell volume changes. These volume changes, confirmed by subsequent in situ XRD experiments, result in structural instability, creating "dead" lithium and poor electrical contact.

In Situ XRD of P-Doped TiO_2. In situ Raman spectroscopy, with its limited penetration depth (typically in the range of a few microns[38,39]), is ideal for studying the surface layer and interface of battery materials. Its analysis focuses on a small area with a radius of about 2 μm, showing that it is sensitive to tiny inhomogeneities in the material lithiation related to the distance to the current collector mesh and electric interaction with the nearby particles. In contrast, in situ XRD has a deeper penetration depth than Raman spectroscopy,[40] often ranging from several microns to tens of microns, and the analysis are performed on a bigger area of the material, around 1.5 cm long and 0.5 cm wide. This makes XRD more suited for investigating overall material characteristics, including crystal structures and phase transitions. In our study, special attention was given to the selection of Raman analysis points, and in situ XRD was performed to gain deeper insights into the reaction mechanisms. In addition, the in situ XRD cell used a higher mass of active material (~15 mg) compared to the in situ Raman cell (~3 mg). A beryllium current collector was used for XRD, differing from the copper mesh used in Raman spectroscopy. To improve the electrical conductivity, 20% Carbon Black was added to the material.

In situ X-ray diffraction patterns recorded during the initial two cycles for each P-doping level are presented (Figure 9). For the nondoped material (Figure 9a), the crystalline peaks of tetragonal TiO_2 are evident, specifically the (101) peak at 25.4° and the (004) peak at 38.1°. These peaks are maintained through the initial voltage drop and a small plateau around 1.75 V. As lithiation progresses, a slight shift and decrease in intensity of the (004) peak are observed until it disappears entirely. Concurrently, a new peak emerges, shifted by approximately 1.7° to higher angles, corresponding to the (004) diffraction peak of $Li_{0.5}TiO_2$. This shift indicates a decrease in the unit cell's c parameter from about 9.42 to 9.03 Å. Simultaneously, the (101) diffraction peak gradually fades, replaced by a new, weaker peak aligning with the (011) peak of the orthorhombic $Li_{0.5}TiO_2$ phase. As lithiation continues, the (004) diffraction peak of $Li_{0.5}TiO_2$ slightly shifts to higher angles and diminishes in intensity. Meanwhile, a new peak, associated with the (004) diffraction peak of $LiTiO_2$, emerges and intensifies in both strength and width, reaching a maximum at the voltage limit of 1 V. The (011) peak transitions back to the (101) peak of $LiTiO_2$ around 24.5°, signifying a structural shift to a tetragonal crystal structure akin

https://doi.org/10.1021/acsomega.3c08122
ACS Omega 2024, 9, 14911−14922

to that of anatase TiO_2. In this $LiTiO_2$ structure, the presence of lithium ions causes the unit cell parameter to expand along the *a* and *b* axes, leading to a reduced unit cell *c* parameter and shifting the (004) peak to higher angles. All three phases exhibit slight peak shifts characteristic of solid-solution behavior, although this effect is minimal for the nondoped material in the first cycle.

During the first charging cycle, the transformation of the material back to TiO_2 is initiated, observable at a voltage increase following a plateau at 1.9 V. However, this transformation exhibits asymmetry compared to the lithiation process. Notably, the (004) peak of $Li_{0.5}TiO_2$ briefly appears during delithiation but with a significantly lower intensity than during lithiation. Additionally, the (011) peak, typically not visible, suggests the emergence of an amorphous behavior in the material. A considerable amount of lithium remains trapped within the material structure and is not fully extracted, as evidenced by the reduced electric capacity during charging and the diminished intensity of the TiO_2 (004) peak compared to its precycling state. This results in lower columbic efficiency. It is important to note that the quantity of lithium extracted from the material closely matches that inserted during the initial transformation step from TiO_2 to $Li_{0.5}TiO_2$. This observation points to the partial irreversibility of lithium insertion in the tetragonal $LiTiO_2$ phase during the first cycle.

In the second cycle of the nondoped material, while the phase transformations mirror those of the first cycle, several differences are noted. The movements of the diffraction peaks indicate more pronounced solid-solution behavior. The Coulombic efficiency in this cycle is improved compared to the first, yet the capacity mirrors that of the initial delithiation. This underscores the likelihood that a significant portion of the material is irreversibly transformed during the first lithiation into the tetragonal $LiTiO_2$ phase, subsequently impeding further lithiation.

In situ XRD results for the various P-doping levels, as shown in Figure 9b–d, reveal that all doping levels undergo the general transformation sequence: $TiO_2 \rightarrow Li_{0.5}TiO_2 \rightarrow LiTiO_2$. However, notable differences are observed among these doping levels. First, materials with P doping achieve deeper lithiation states, evidenced by both the calculated capacities and the increased intensity of the (004) peak of the tetragonal $LiTiO_2$ phase. This is particularly pronounced in the 10% P-doped material, which also exhibits a more significant peak shift. Second, the Coulombic efficiency in the first cycle shows considerable improvement across P-doped samples, suggesting a reduction in the kinetic barriers associated with the third phase, $LiTiO_2$. Moreover, the diffraction peaks of the orthorhombic $Li_{0.5}TiO_2$ phase become more pronounced during delithiation, which is especially noticeable in the 2% P-doped sample. This observation points to a minimized disparity in phase transformations between charging and discharging.

These in situ XRD findings corroborate the results obtained from in situ Raman experiments. They particularly highlight the enhanced depth of lithiation in P-doped materials and the improvement in first-cycle Coulombic efficiency due to more reversible phase transformations.

DISCUSSION

Doped TiO_2 materials, including those with P doping, have demonstrated superior lithium-ion storage capacity and rate performance compared to undoped TiO_2. Additionally, doping has been found to increase the electrochemical stability of TiO_2.[41−44] However, detailed studies on the phase transformation mechanism and control of lithium insertion-extraction processes have been limited. According to our in situ Raman spectroscopy and XRD analyses (Figures 3 and 9), P-doped TiO_2 anatase materials achieve higher lithiation levels during the first discharge process compared to nondoped TiO_2. In nondoped TiO_2, the formation of the $LiTiO_2$ phase on particle surfaces hinders higher lithiation states due to its low electronic conductivity. In contrast, P doping significantly enhances the conductivity of $LiTiO_2$, facilitating deeper lithiation states and higher initial specific capacities.

This study highlights the impact of P doping on the reversibility of lithiation/delithiation reactions. Nondoped TiO_2 does not revert completely to its initial structure at the end of the first cycle, with orthorhombic $Li_{0.5}TiO_2$ coexisting with anatase TiO_2. However, for 2% and 5% P-doped TiO_2, the anatase phase is fully recoverable at the end of charging in the initial four cycles, demonstrating enhanced reaction reversibility. Nonetheless, traces of the tetragonal $LiTiO_2$ phase are detectable in 10% P-doped TiO_2.

Through hierarchical clustering applied to in situ data, we successfully identified separate phases during the double phase transformation "tetragonal $TiO_2 \leftrightarrow$ orthorhombic $Li_{0.5}TiO_2 \leftrightarrow$ tetragonal $LiTiO_2$". For the first time, we can distinctly identify the Raman spectra of the Li-rich $LiTiO_2$ phase. Additionally, our analysis reveals that nonreversible lithium ions trapped in the structure impose stress, as evidenced by the red shift and decreased vibrational energy in the B_{2g}, B_{3g} bands.

The P-doping of TiO_2 was found to decrease the crystallite size and increases the material conductivity, which was shown by the bands broadening and blue shifts.

The incorporation of phosphorus in TiO_2 leads to a reduction in the crystallite size and an increase in the material conductivity. This change is reflected in the broadening and blue shifting of the Raman bands. Initially, P-doping results in a red shift and broadening of these bands, correlating with reduced crystallite size and enhanced conductivity. However, upon cycling, a lithiation-triggered effect emerges, characterized by a blue shift in the bands. The interplay between the stress induced by trapped lithium and the lithiation-triggered effect of phosphorus doping creates a dynamic equilibrium. An optimal P-doping level is suggested, where phosphorus alleviates the stress induced by lithiation. Nevertheless, it is observed that higher doping levels may reintroduce stress into the material.

CONCLUSIONS

This study provides critical insights into the effects of phosphorus (P) doping on the electrochemical behavior of titanium dioxide (TiO_2) in lithium-ion batteries. Key findings include the enhanced lithiation capability of P-doped TiO_2, with in situ Raman spectroscopy and XRD analyses revealing higher lithiation levels in P-doped materials compared to nondoped counterparts. This enhancement is attributed to the improved conductivity of the $LiTiO_2$ phase due to P doping, which facilitates deeper lithiation and higher initial specific capacities.

A significant improvement in the reversibility of lithiation/delithiation reactions was observed in P-doped TiO_2. While nondoped TiO_2 exhibited incomplete reversibility, P-doped TiO_2, particularly at 2% and 5% doping levels, demonstrated a more reversible recovery of the anatase phase during the initial

https://doi.org/10.1021/acsomega.3c08122
ACS Omega 2024, 9, 14911−14922

cycles. The study also highlighted the contrasting effects of trapped lithium and P doping on the vibrational modes of TiO_2, with an optimal P-doping level at around 3.3 wt % that balances these effects to enhance overall electrochemical performance.

These findings have important implications for the development of TiO_2-based anodes in lithium-ion batteries. The enhanced understanding of phase transformations and conductivity improvements through P doping opens avenues for designing more efficient and durable anode materials, potentially leading to batteries with greater capacities and longer life cycles.

METHODS

Materials Preparation. Anatase titanium oxide TiO_2 and P-doped TiO_2 nanoparticles were synthesized using the sol–gel method, following the procedure outlined by Karim et al.[22,45] A volume V1 of titanium(IV) isopropoxide solution (99.999% trace metals base, Sigma-Aldrich) was mixed with 100 mL of ethanol absolute (Sigma-Aldrich), and then a volume V2 of phosphoric acid solution was added to the mixture (Sigma-Aldrich) under magnetic stirring. Table 1 presents the volumes for each doping level.

Table 1. Synthesis Volumes for Each P-Doping Level

doping level	V1 (titanium isopropoxide) [mL]	V2 (phosphoric acid) [μL]
0%	9.77	0
2%	9.72	43
5%	9.66	108
10%	9.55	216

Alginate solution was prepared by dissolving 1 g of sodium alginate powder in 100 mL of distilled water before being added dropwise to the first solution. The mixture was stirred for three h at room temperature. The solid was collected after being repeatedly centrifuged at 10.000 rpm for 10 min and washed with distilled water. The powder was dried for a whole night at 120 °C then calcined at 400 °C for 5 h to crystallize both TiO_2 and the P-TiO_2 nanoparticles.

Electrochemical Analysis and In Situ Cell Assembly. The electrodes were assembled in an argon-filled glovebox, using an in situ EL-Cell (ECC-Opto-Std EL-CELL) with a sapphire optical window designed to perform the spectro-electrochemical investigation of the P-doped and undoped TiO_2 electrodes without any additive, a freshly cut and cleaned Li metal disk was used as a counter electrode, a glass fiber separator (ECC1–01–0012-J/L EL-CELL) soaked in an electrolyte of 1 mol·L^{-1} $LiPF_6$ dissolved in 1:1 ethylene carbonate (EC)-dimethyl carbonate (DMC) (Sigma-Aldrich).[46] The cell was left to rest overnight in an OCV. Galvanostatic cycling with potential limitation (GCPL) was performed between 1 and 3 V vs Li/Li^+ at a C-rate of C/20 using a Biologic SP150 potentiostat. During cycling, Raman spectroscopy measurements were recorded using a Raman spectrometer LabRAM HR evolution (Horiba Scientific), with a confocal microscope (×50) objective, and a spectrometer with a grating of 1800 lines/mm grating, with an excitation wavelength of 532 nm, 50s exposure time and two accumulations for each spectrum. The experiments were performed at room temperature of 22 °C. Crystal structure of the products was measured on a Bruker D8 Advance X-ray diffractometer (XRD) with Cu K radiation (λ = 1.5418 Å). The same equipment was used for in situ measurements, the XRD spectrum was recorded every 30 min while the material was being charged and discharged. A high-resolution scanning electron microscope (SEM) (EVO 10, ZEISS) was used to examine the morphology of the synthetic cobalt-free cathode material. Prior to SEM inspection, the sample's surface was coated with carbon while being held in a high vacuum for 20 min in a sputtering coater.

Data Analysis. Data analysis was conducted using a custom Python code. This code utilized libraries such as pandas, numpy, matplotlib, mpl_toolkits, peakutils, csv, scipy, and sklearn for data handling, processing, and analysis. This encompassed tasks such as reading, organizing, smoothing, interpolating, normalizing, peak detection in Raman spectroscopy data, and applying linear regression and hierarchical clustering models for in-depth analysis.

ASSOCIATED CONTENT

Supporting Information

The Supporting Information is available free of charge at https://pubs.acs.org/doi/10.1021/acsomega.3c08122.

SEM images, the peak fitting results in addition to the capacity retention for all P-doped material (PDF)

AUTHOR INFORMATION

Corresponding Author

Mouad Dahbi − *Materials Science and Nano-engineering Department, Mohammed VI Polytechnic University, Ben Guerir 43150, Morocco;* orcid.org/0000-0001-8165-4812; Email: mouad.dahbi@um6p.ma

Authors

Ayoub El Bendali − *Materials Science and Nano-engineering Department, Mohammed VI Polytechnic University, Ben Guerir 43150, Morocco*

Mohamed Aqil − *Materials Science and Nano-engineering Department, Mohammed VI Polytechnic University, Ben Guerir 43150, Morocco*

Loubna Hdidou − *Materials Science and Nano-engineering Department, Mohammed VI Polytechnic University, Ben Guerir 43150, Morocco*

Nabil El Halya − *Materials Science and Nano-engineering Department, Mohammed VI Polytechnic University, Ben Guerir 43150, Morocco*

Karim El Ouardi − *Materials Science and Nano-engineering Department, Mohammed VI Polytechnic University, Ben Guerir 43150, Morocco*

Jones Alami − *Materials Science and Nano-engineering Department, Mohammed VI Polytechnic University, Ben Guerir 43150, Morocco*

Davide Boschetto − *CNRS, Ecole Polytechnique, ENSTA Paris, Institut Polytechnique de Paris, LOA, Laboratoire d'Optique Appliquée, Palaiseau 91120, France*

Complete contact information is available at: https://pubs.acs.org/10.1021/acsomega.3c08122

Notes

The authors declare no competing financial interest.

https://doi.org/10.1021/acsomega.3c08122
ACS Omega 2024, 9, 14911−14922

■ ACKNOWLEDGMENTS

The authors would like to thank Office Chérifien des Phosphates (OCP S.A.) and Mohammed VI Polytechnic University for financial support.

■ REFERENCES

(1) Armand, M.; Tarascon, J.-M. Building Better Batteries. *Nature* **2008**, *451* (7179), 652−657.
(2) Scrosati, B.; Garche, J. Lithium Batteries: Status. *Prospects and Future. J. Power Sources* **2010**, *195* (9), 2419−2430.
(3) Baazizi, M.; Dahbi, M.; Aqil, M.; Ghamouss, F.; Saadoune, I.A Ni-Rich Cathode Material for Lithium-Ion Batteries with Improved Safety and Cost. In *2019 7th International Renewable and Sustainable Energy Conference (IRSEC)*; IEEE, 2019; pp 1−4. DOI: 10.1109/IRSEC48032.2019.9078158.
(4) Goodenough, J. B.; Kim, Y. Challenges for Rechargeable Li Batteries. *Chem. Mater.* **2010**, *22* (3), 587−603.
(5) Ellis, B. L.; Lee, K. T.; Nazar, L. F. Positive Electrode Materials for Li-Ion and Li-Batteries. *Chem. Mater.* **2010**, *22* (3), 691−714.
(6) Aqil, M.; Aqil, A.; Ouhib, F.; El Idrissi, A.; Dahbi, M.; Detrembleur, C.; Jérôme, C. Nitroxide TEMPO-Containing PILs: Kinetics Study and Electrochemical Characterizations. *Eur. Polym. J.* **2021**, *152*, No. 110453.
(7) Wagemaker, M.; Borghols, W. J. H.; Mulder, F. M. Large Impact of Particle Size on Insertion Reactions. A Case for Anatase Li x TiO 2. *J. Am. Chem. Soc.* **2007**, *129* (14), 4323−4327.
(8) Borghols, W. J. H.; Lützenkirchen-Hecht, D.; Haake, U.; van Eck, E. R. H.; Mulder, F. M.; Wagemaker, M. The Electronic Structure and Ionic Diffusion of Nanoscale LiTiO2 Anatase. *Phys. Chem. Chem. Phys.* **2009**, *11* (27), 5742.
(9) Aqil, A.; El Kadib, A.; Aqil, M.; Bousmina, M.; Elidrissi, A.; Detrembleur, C.; Jérôme, C. Nitroaldol Condensation Catalyzed by Topologically Modulable Cooperative Acid-Base Chitosan-TiO2 Hybrid Materials. *RSC Adv.* **2014**, *4* (63), 33160−33163.
(10) Lee, D.-H.; Lee, B.-H.; Sinha, A. K.; Park, J.-H.; Kim, M.-S.; Park, J.; Shin, H.; Lee, K.-S.; Sung, Y.-E.; Hyeon, T. Engineering Titanium Dioxide Nanostructures for Enhanced Lithium-Ion Storage. *J. Am. Chem. Soc.* **2018**, *140* (48), 16676−16684.
(11) Gentili, V.; Brutti, S.; Hardwick, L. J.; Armstrong, A. R.; Panero, S.; Bruce, P. G. Lithium Insertion into Anatase Nanotubes. *Chem. Mater.* **2012**, *24* (22), 4468−4476.
(12) Lin, D.; Lyu, L.; Li, K.; Chen, G.; Yao, H.; Kang, F.; Li, B.; Zhou, L. Ultrahigh capacity and cyclability of dual-phase TiO 2 nanowires with low working potential at room and subzero temperatures. *J. Mater. Chem. A* **2021**, *9*, 9256−9265.
(13) Zheng, J.; Liu, L.; Ji, G.; Yang, Q.; Zheng, L.; Zhang, J. Hydrogenated Anatase TiO 2 as Lithium-Ion Battery Anode: Size−Reactivity Correlation. *ACS Appl. Mater. Interfaces* **2016**, *8* (31), 20074−20081.
(14) Li, X.; Zhang, F.; Zhai, B.; Wang, X.; Zhao, J.; Wang, Z. Facile Synthesis of Porous Anatase TiO2 Nanomaterials with the Assistance of Biomass Resource for Lithium Ion Batteries with High-Rate Performance. *J. Phys. Chem. Solids* **2020**, *145* (March), No. 109552.
(15) Wu, F.; Wang, Z.; Li, X.; Guo, H. Simple Preparation of Petal-like TiO 2 Nanosheets as Anode Materials for Lithium-Ion Batteries. *Ceram. Int.* **2014**, *40* (10), 16805−16810.
(16) Armstrong, A. R.; Armstrong, G.; Canales, J.; García, R.; Bruce, P. G. Lithium-Ion Intercalation into TiO 2 -B Nanowires. *Adv. Mater.* **2005**, *17* (7), 862−865.
(17) Wu, Q.; He, S.; Yang, X.; Yang, J.; Li, G.; Meng, Y.; Tong, S.; Mai, L.; Wu, M. Ultrathin Nanobelts-Assembled Chinese Knot-like 3D TiO2 for Fast and Stable Lithium Storage. *Nano Res.* **2018**, *11* (4), 2116−2128.
(18) Opra, D. P.; Gnedenkov, S. V.; Sinebryukhov, S. L.; Voit, E. I.; Sokolov, A. A.; Ustinov, A. Y.; Zheleznov, V. V. Zr4+/F− Co-Doped TiO2(Anatase) as High Performance Anode Material for Lithium-Ion Battery. *Prog. Nat. Sci. Mater. Int.* **2018**, *28* (5), 542−547.
(19) Zhao, J.; Wei, D.; Zhang, X.; Zhang, S.; Zhang, C.; Yang, X. Biomass-Derived Hierarchical N, P Codoped Porous 3D-Carbon Framework@TiO2 Hybrids as Advanced Anode for Lithium Ion Batteries. *J. Colloid Interface Sci.* **2022**, *606*, 577−587.
(20) Kyeremateng, N. A.; Vacandio, F.; Sougrati, M.-T.; Martinez, H.; Jumas, J.-C.; Knauth, P.; Djenizian, T. Effect of Sn-Doping on the Electrochemical Behaviour of TiO2 Nanotubes as Potential Negative Electrode Materials for 3D Li-Ion Micro Batteries. *J. Power Sources* **2013**, *224*, 269−277.
(21) Madhusudanan, S. P.; Gangaja, B.; Shyla, A. G.; Nair, A. S.; Nair, S. V.; Santhanagopalan, D. Sustainable Chemical Synthesis for Phosphorus-Doping of TiO2 Nanoparticles by Upcycling Human Urine and Impact of Doping on Energy Applications. *ACS Sustain. Chem. Eng.* **2017**, *5* (3), 2393−2399.
(22) El Halya, N.; Aqil, M.; El Ouardi, K.; Bano, A.; El Bendali, A.; Hdidou, L.; Amine, R.; Son, S.-B.; Ghamouss, F.; Major, D. T.; Amine, K.; Alami, J.; Dahbi, M. Biopolymer-assisted Synthesis of P-doped TiO2 Nanoparticles for High-performance Lithium-ion Batteries: A Comprehensive Study. *Batteries Supercaps* **2023**, No. e202300424, DOI: 10.1002/batt.202300424.
(23) Ceballos-Chuc, M. C.; Ramos-Castillo, C. M.; Alvarado-Gil, J. J.; Oskam, G.; Rodríguez-Gattorno, G. Influence of Brookite Impurities on the Raman Spectrum of TiO2 Anatase Nanocrystals. *J. Phys. Chem. C* **2018**, *122* (34), 19921−19930.
(24) Hardwick, L. J.; Holzapfel, M.; Novák, P.; Dupont, L.; Baudrin, E. Electrochemical Lithium Insertion into Anatase-Type TiO2: An in Situ Raman Microscopy Investigation. *Electrochim. Acta* **2007**, *52* (17), 5357−5367.
(25) de Klerk, N. J. J.; Vasileiadis, A.; Smith, R. B.; Bazant, M. Z.; Wagemaker, M. Explaining Key Properties of Lithiation in TiO2-Anatase Li-Ion Battery Electrodes Using Phase-Field Modeling. *Phys. Rev. Mater.* **2017**, *1* (2), No. 025404.
(26) Koyanagi, T.; Lance, M. J.; Katoh, Y. Quantification of Irradiation Defects in Beta-Silicon Carbide Using Raman Spectroscopy. *Scr. Mater.* **2016**, *125*, 58−62.
(27) Xue, X.; Ji, W.; Mao, Z.; Mao, H.; Wang, Y.; Wang, X.; Ruan, W.; Zhao, B.; Lombardi, J. R. Raman Investigation of Nanosized TiO 2: Effect of Crystallite Size and Quantum Confinement. *J. Phys. Chem. C* **2012**, *116* (15), 8792−8797.
(28) El-Deen, S. S.; Hashem, A. M.; Abdel Ghany, A. E.; Indris, S.; Ehrenberg, H.; Mauger, A.; Julien, C. M. Anatase TiO2 Nanoparticles for Lithium-Ion Batteries. *Ionics (Kiel).* **2018**, *24* (10), 2925−2934.
(29) Laskova, B.; Frank, O.; Zukalova, M.; Bousa, M.; Dracinsky, M.; Kavan, L. Lithium Insertion into Titanium Dioxide (Anatase): A Raman Study with 16/18 O and 6/7 Li Isotope Labeling. *Chem. Mater.* **2013**, *25* (18), 3710−3717.
(30) Ai, Y. J.; Liang, P.; Wu, Y. X.; Dong, Q. M.; Li, J. B.; Bai, Y.; Xu, B. J.; Yu, Z.; Ni, D. Rapid Qualitative and Quantitative Determination of Food Colorants by Both Raman Spectra and Surface-Enhanced Raman Scattering (SERS). *Food Chem.* **2018**, *241*, 427−433.
(31) Gold-Parker, A.; Gehring, P. M.; Skelton, J. M.; Smith, I. C.; Parshall, D.; Frost, J. M.; Karunadasa, H. I.; Walsh, A.; Toney, M. F. Acoustic Phonon Lifetimes Limit Thermal Transport in Methylammonium Lead Iodide. *Proc. Natl. Acad. Sci. U. S. A.* **2018**, *115* (47), 11905−11910.
(32) Ma, B.; Rodriguez, R. D.; Ruban, A.; Pavlov, S.; Sheremet, E. The Correlation between Electrical Conductivity and Second-Order Raman Modes of Laser-Reduced Graphene Oxide. *Phys. Chem. Chem. Phys.* **2019**, *21* (19), 10125−10134.
(33) Slobodian, O. M.; Tiagulskyi, S. I.; Nikolenko, A. S.; Stubrov, Y.; Gomeniuk, Y. V.; Lytvyn, P. M.; Nazarov, A. N. Micro-Raman Spectroscopy and Electrical Conductivity of Graphene Layer on SiO 2 Dielectric Subjected to Electron Beam Irradiation. *Mater. Res. Express* **2018**, *5* (11), No. 116405.
(34) Fung, A. W. P.; Rao, A. M.; Kuriyama, K.; Dresselhaus, M. S.; Dresselhaus, G.; Endo, M.; Shindo, N. Raman Scattering and Electrical Conductivity in Highly Disordered Activated Carbon Fibers. *J. Mater. Res.* **1993**, *8* (3), 489−500.

https://doi.org/10.1021/acsomega.3c08122
ACS Omega 2024, 9, 14911−14922

(35) Matadi, B. P.; Geniès, S.; Delaille, A.; Chabrol, C.; de Vito, E.; Bardet, M.; Martin, J.-F.; Daniel, L.; Bultel, Y. Irreversible Capacity Loss of Li-Ion Batteries Cycled at Low Temperature Due to an Untypical Layer Hindering Li Diffusion into Graphite Electrode. *J. Electrochem. Soc.* **2017**, *164* (12), A2374−A2389.
(36) Pender, J. P.; Jha, G.; Youn, D. H.; Ziegler, J. M.; Andoni, I.; Choi, E. J.; Heller, A.; Dunn, B. S.; Weiss, P. S.; Penner, R. M.; Mullins, C. B. Electrode Degradation in Lithium-Ion Batteries. *ACS Nano* **2020**, *14* (2), 1243−1295.
(37) Ventosa, E.; Madej, E.; Zampardi, G.; Mei, B.; Weide, P.; Antoni, H.; La Mantia, F.; Muhler, M.; Schuhmann, W. Solid Electrolyte Interphase (SEI) at TiO2 Electrodes in Li-Ion Batteries: Defining Apparent and Effective SEI Based on Evidence from X-Ay Photoemission Spectroscopy and Scanning Electrochemical Microscopy. *ACS Appl. Mater. Interfaces* **2017**, *9* (3), 3123−3130.
(38) Borowicz, P. Depth-Sensitive Raman Investigation of Metal-Oxide-Semiconductor Structures: Absorption as a Tool for Variation of Exciting Light Penetration Depth. *J. Spectrosc.* **2016**, *2016*, No. 1617063.
(39) Julien, C. M.; Mauger, A. In Situ Raman Analyses of Electrode Materials for Li-Ion Batteries. *AIMS Mater. Sci.* **2018**, *5* (4), 650−698, DOI: 10.3934/matersci.2018.4.650.
(40) Manova, D.; Mändl, S. In Situ XRD Measurements to Explore Phase Formation in the near Surface Region. *J. Appl. Phys.* **2019**, *126* (20), No. 200901.
(41) Huo, J.; Xue, Y.; Wang, X.; Liu, Y.; Zhang, L.; Guo, S. TiO2/Carbon Nanofibers Doped with Phosphorus as Anodes for Hybrid Li-Ion Capacitors. *J. Power Sources* **2020**, *473*, No. 228551.
(42) Kashale, A. A.; Rasal, A. S.; Kamble, G. P.; Ingole, V. H.; Dwivedi, P. K.; Rajoba, S. J.; Jadhav, L. D.; Ling, Y.-C.; Chang, J.-Y.; Ghule, A. V. Biosynthesized Co-Doped TiO2 Nanoparticles Based Anode for Lithium-Ion Battery Application and Investigating the Influence of Dopant Concentrations on Its Performance. *Compos. Part B Eng.* **2019**, *167*, 44−50.
(43) El Halya, N.; Elouardi, K.; Chari, A.; El Bouari, A.; Alami, J.; Dahbi, M. TiO 2 Based Nanomaterials and Their Application as Anode for Rechargeable Lithium-Ion Batteries. In *Titanium Dioxide - Advances and Applications*; IntechOpen, 2022. DOI: 10.5772/intechopen.99252.
(44) Zhao, X.-C.; Yang, P.; Yang, L.-J.; Cheng, Y.; Chen, H.-Y.; Liu, H.; Wang, G.; Murugadoss, V.; Angaiah, S.; Guo, Z. Enhanced Electrochemical Performance of Cu2+ Doped TiO2 Nanoparticles for Lithium-Ion Battery. *ES Mater. Manuf.* **2018**, *1*, 67−71.
(45) El Ouardi, K.; Dahbi, M.; Hakim, C.; Güler, M. O.; Akbulut, H.; El Bouari, A.; Saadoune, I. Facile Synthesis of Nanoparticles Titanium Oxide as High-Capacity and High-Capability Electrode for Lithium-Ion Batteries. *J. Appl. Electrochem.* **2020**, *50* (5), 583−595.
(46) Baazizi, M.; Karbak, M.; Aqil, M.; Sayah, S.; Dahbi, M.; Ghamouss, F. High-Valence Surface-Modified LMO Cathode Materials for Lithium-Ion Batteries: Diffusion Kinetics and Operando Thermal Stability Investigation. *ACS Appl. Mater. Interfaces* **2023**, *15* (34), 40385−40396.

https://doi.org/10.1021/acsomega.3c08122
ACS Omega 2024, 9, 14911−14922